PCCP

A ReaxFF Molecular Dynamics Study of Molecular-Level Interactions During Binder Jetting 3D-Printing

Journal:	*Physical Chemistry Chemical Physics*
Manuscript ID	CP-ART-06-2019-003585.R1
Article Type:	Paper
Date Submitted by the Author:	20-Aug-2019
Complete List of Authors:	Gao, Yawei; Pennsylvania State University University Park, Mechanical Engineering Shin, Yun Kyung; Pennsylvania State University, Mechanical and Nuclear Engineering Martinez, Daniel; Pennsylvania State University University Park, Mechanical Engineering Manogharan, Guha; Pennsylvania State University University Park, Mechanical Engineering van Duin, Adri; The Pennsylvania State University, Mechanical and Nuclear Engineering

SCHOLARONE™
Manuscripts

PCCP

ARTICLE TYPE

Cite this: DOI: 00.0000/xxxxxxxxxx

A ReaxFF Molecular Dynamics Study of Molecular-Level Interactions During Binder Jetting 3D-Printing

Yawei Gao, Yun Kyung Shin, Daniel Martinez, Guha Manogharan, and Adri C.T. van Duin*

Received Date
Accepted Date

DOI: 00.0000/xxxxxxxxxx

In the present work, we study one of the major additive manufacturing process, *i.e.*, the binder jetting print (BJP) process at the molecular level through atomistic-scale level representations of powders and binder solutions with chromium-oxide (Cr-oxide) nanoparticles and water-based diethylene glycol solutions, respectively. Results show that both diethylene glycol and water contribute to the bonding of Cr-oxide particles during the print and curing stages by forming a hydrogen bond network. Heating the system to the burn-out temperature results in the oxidation of diethylene glycol and the decomposition of the hydrogen bond network. Subsequently, Cr-oxide particles are partially sintered by forming Cr-O bonds. The final sintering facilitates further Cr-O bond formation. Additionally, the influence of the chemical composition of the binder solution is investigated by performing ReaxFF molecular dynamics simulations on two sets of systems, which control the number of water and diethylene glycol molecules, respectively. Our results demonstrate that adding both diethylene glycol and water in the binder solution can raise the number of "useful" hydrogen bonds, resulting in a higher breaking strength at the print and curing stages. During the burn-out and sintering stages, the influence of water on the breaking strength is not obvious. In contrast, an optimal quantity of binder species exists for the breaking strength after sintering. A comparison of the ReaxFF molecular dynamics simulations using 2-ethoxyethanol, diethylene glycol and 1-(2,2,2-trihydroxyethoxy)ethane-2,2,2-triol as the binder phase indicates that an increasing number of hydroxyl groups leads to higher breaking strength at the print and curing stages. Findings from this study can be extended to identify optimal binder chemistry, curing and sintering conditions for different material systems.

Introduction

Additive manufacturing (AM) has demonstrated its advantages over traditional manufacturing technologies. AM generates less scrap, reduces the time for a final part delivery, and fabricate complex shapes that are difficult to produce via conventional routes.[1] Binder jetting print (BJP) is a notable powder bed based AM processes category, which decouples the print and consolidation, enabling us to fabricate products with uniform final microstructures.[2] The general process flow of a BJP cycle is shown in Fig. 1. During the print stage, the roller spreads powders from the supply bed to the build platform layer by layer. Meanwhile, the print head selectively deposits the binder solution into the powder bed across cross-sections that are intended to be consolidated. The volume of the injected binder solution is controlled by the parameter binder saturation S, which is based on the estimation of binder packing density:

$$S = \frac{V_{\text{binder}}}{V_{\text{air}}}, \tag{1}$$

where V_{binder} and V_{air} represent the volume of binder solution and pores in the powder bed, respectively.[1] It should be noted that this study does not include the secondary operation of infiltration that is employed in certain applications to improve overall density and mechanical strength.[3,4] Following the print stage, the BJP sample is placed in an oven and heated to cure the binder phase. Before burning the binder phase at a higher temperature, loose powders are removed from the build platform. After the burn-out stage, the printed sample is transferred into an environment-controlled oven for final sintering.[2] The main weakness of BJP is that high density is often difficult to achieve.[2] Nandwana *et al.*[1] compared the microstructure of BJP samples using 7 μm, 21 μm and 70 μm powders and found that smaller size particles densify at a higher rate. Miyanaji *et al*[5] developed a physics-based model to estimate the optimal saturation for a

Department of Mechanical Engineering, The Pennsylvania State University, University Park, PA 16802, USA. Tel: +1 814 863 6277; E-mail: acv13@psu.edu

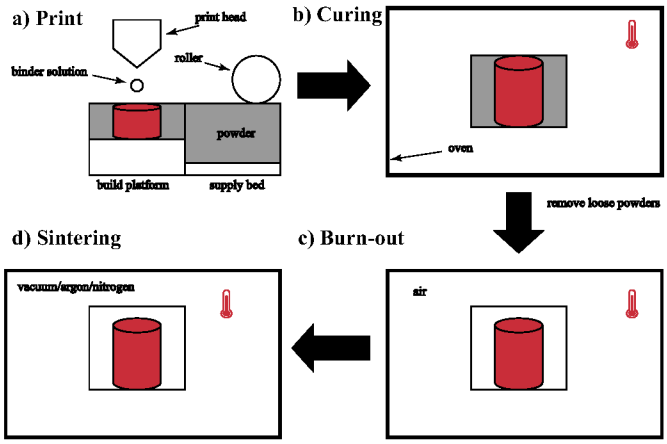

Fig. 1 The BJP procedure.

BJP process and discovered that the permeation of the binder solution is driven by both the excess pressure and the capillary pressure and that the equilibrium conditions are determined by the capillary pressure. Doyle *et al.*[6] investigated the effects of layer thickness and orientation on mechanical properties and showed that the layer thickness has a larger degree of influence on mechanical properties than orientation. Moon *et al.*[7] discovered that the binder infiltration behavior is determined by molecular weight, surface tension, and viscosity of binders as well as the pore size of powder beds. While reported studies are primarily based on experimental approaches, the fundamental mechanisms of BJP have not been fully understood, especially the underlying physical and chemical changes at a molecular level during a BJP cycle.

The present work introduces a model for the BJP process. This model, which contains organic and inorganic species, provides a molecular-level explanation for mechanical property evolution at different stages. We apply this model to study the BJP process using AISI 316 L stainless steel powders. AISI 316 L stainless steel has intrinsic corrosion resistance due to its passivation layer that is rich in chromium oxide (Cr_2O_3).[8–10] Thus, we employ a Cr/C/H/O force field provided by Shin *et al.*[11] Based on this force field, MD simulations at 300 K, 393 K, 900 K, and 1900 K are carried out on a system with two nanoparticles simulating surfaces of two powder particles and numerous binder molecules. The motivation for analyzing MD simulations is to better understand how a BJP sample gains strength during a BJP process. It must be noted that a one-to-one agreement between the ReaxFF results and AM experiments is not realistic, given the disparity of time and length scales of ReaxFF reactive force field method (picoseconds to nanoseconds/angstrom to nanometer) and those of experiments (minutes to hours/above 1 micrometer).

In addition, experiments have confirmed that a higher level of saturation results in a stronger green part at the print and curing stages (the green part is a term used in powder metallurgy to describe a part that needs to be further processed), while oversaturation weakens the sintered sample,[12–15] but there is a critical gap in literature that explains the underlying physical and chemical mechanism of this correlation. In principle, a higher saturation level can be achieved by adding either water or binder species. However, it is unknown which species in the binder solution is more effective in gaining strengths. For that, we perform multiple ReaxFF MD simulations on systems with a varying number of binder species and water molecules, in order to study the influence of the chemical compositions of binder solutions on mechanical properties. It must be noted that mechanical properties include numerous indicators such as ductility, viscosity, *etc.* In this present work, we primarily focus on breaking strength, unless otherwise noted.

Additionally, we also compare breaking strengths using 2-ethoxyethanol, diethylene glycol (DEG) and 1-(2,2,2-trihydroxyethoxy)ethane-2,2,2-triol as the binder phase with the ReaxFF MD method to investigate the significance of the number of hydroxyl groups. This investigation contributes to understanding the influence of the molecular structure of binder species on mechanical properties, which can serve as a basis for the development of new binder solutions.

Simulation Methods

ReaxFF reactive force field method

The ReaxFF reactive force field method was developed for exploring, developing and optimizing material properties. It bridges quantum mechanical and empirical computational methods. The interatomic potential in the ReaxFF reactive force field method employs a bond-order based formalism, which allows ReaxFF to describe both covalent and electrostatic interactions. The ReaxFF potentials are summarized by:[16]

$$E_{\text{system}} = E_{\text{bond}} + E_{\text{over}} + E_{\text{angle}} + E_{\text{tors}} + E_{\text{vdWaals}} + E_{\text{Coulumb}} + E_{\text{specific}}. \quad (2)$$

E_{bond} is the energy associated with forming bonds, which is a continuous function based on the interatomic distance. E_{angle} and E_{tors} are the energies associated with valence angle and torsional angle. E_{over} is the energy penalty preventing the overcoordination of atoms, which is based on atomic valence rules. E_{Coulumb} and E_{vdWaals} are electrostatic and London dispersive energy contributions. E_{specific} represents system specific terms such as lone-pair, conjugation, hydrogen binding and C_2 corrections.[16] A more detailed introduction to the ReaxFF reactive force method is available in other literature.[17–20]

Setups of the ReaxFF MD simulations

In order to study the physical and chemical evolution of AISI 316 L stainless steel powders during a BJP cycle, which has a Cr_2O_3 layer as a protective film on the surface, we prepare a system consisting of Cr-oxide powders and binder solutions (DEG and water).[1,3,10] It must be noted that the diameters of the powders in experiments are usually in approximately 10 μm $\sim$ 100 μm range,[1,15,21] while in this present work, the powders are approximately 22 Å in diameter and have merely around 500 atoms. As such, we do not expect a one-to-one agreement between experiments and MD simulations. Instead, we aim to relate mechanical

Table 1 Chemical compositions of binder solutions

Set A	Set B
80 water + 60 DEG	240 water + 20 DEG
160 water + 60 DEG	240 water + 60 DEG
240 water + 60 DEG	240 water +100 DEG

properties development with the physical and chemical evolution at the molecular level. Hence, such a system only needs to be large enough to describe the reactions between the powder surface, DEG, and water. In order to prepare the powder material, a Cr-oxide nanoparticle of roughly 500 atoms must be annealed and subsequently equilibrated in an environment of H_2O and O_2 at 1273 K to create a saturated surface that is rich in oxygen, reducing the surface energy of the Cr-oxide nanoparticle. Subsequently, we distribute 2 equilibrated Cr-oxide nanoparticles, 160 water, and 60 DEG molecules randomly in an 80 Å × 80 Å × 80 Å periodic cell, as shown in Fig. S1. The periodic boundary condition keeps the system from losing any water or DEG molecules during the print stage. Then, ReaxFF MD simulations at 300 K are performed to simulate the print stage, using the canonical ensemble (NVT), where the number of particles (N), temperature (T) and volume (V) are constant.[22] A Berendsen thermostat with a temperature damping constant of 100 fs is employed. Prior to the simulation of the curing stage, the size of the simulation cell is expanded to 200 Å × 200 Å × 200 Å to simulate a non-periodic environment, as shown in Fig. S2. NVT-MD simulation at 393 K is carried out to simulate the curing process.[23–25] At this temperature, water molecules evaporate and all dissociated water molecules are therefore removed after curing. Subsequently, we carry out NVT-MD simulations of 900 K in the system to burn out the binder phase.[1] DEG molecules decompose at this temperature and all gaseous species are removed after the burn-out stage. For sintering, we perform NVT-MD simulations of 1900 K.[26–28] At the beginning of each stage, the system is directly heated to the desired temperature. The influence of heating methods is beyond the scope of this work.

In this present work, we primarily investigate breaking strength, one of the most vital indicators of mechanical properties. The breaking strength is reflected by the energy barrier to separate the two Cr-oxide particles, which is calculated by adding an additional force to the ReaxFF potential. This force features an upside-down bell curve and is shown as[29]

$$E_{\text{restraint}} = F_1 - F_1 \exp\left[F_2 \left(R_{ij} - R_{12}\right)^2\right], \tag{3}$$

where F_1 and F_2 are the force constants of the additional force. R_{ij} is the distance between atoms i and j, while R_{12} is a value updating every iteration. By increasing or decreasing R_{12}, atoms i and j are pulled apart or together correspondingly. We can also control the strain rate by adjusting R_{12}/iteration. In the present work, the applied additional force is exerted equally on 50 atoms pairs. The two atoms of each pair are selected from different nanoparticles. This set-up ensures that the added external force separates the two Cr-oxide particles instead of breaking off any individual atom.

In order to study the effect of chemical compositions of binder solutions on the breaking strength, we prepare two sets of simulations shown in Tab. 1. Set A is to study the influence of water, while Set B is to investigate the role of DEG. Theoretically, the model is able to simulate a system with more than two Cr-oxide nanoparticles, but the configuration effect with over two particles is hard to quantify. For example, the configuration in Fig. S3a is akin to a chain, which is significantly weaker than the configuration shown in Fig. S3b. With such a strong impact of the configuration, it is hard to compare the effect of chemical composition. Therefore, only two nanoparticles are used to reduce the influence of configuration. Additionally, 5 cases similar to Fig. S1 are prepared unbiasedly for each chemical composition, in order to reduce the configuration bias. NVT-MD simulations at 300 K, 393 K, 900 K, and 1900 K are performed also unbiasedly for each case. The average breaking strengths and the error bars based on the equilibrium states of the 5 cases are compared for each temperature.

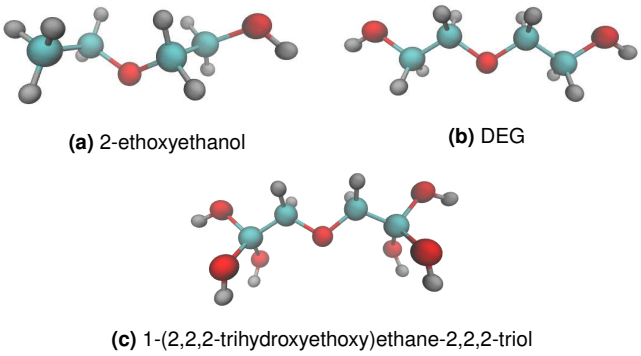

(a) 2-ethoxyethanol **(b)** DEG

(c) 1-(2,2,2-trihydroxyethoxy)ethane-2,2,2-triol

Fig. 2 Molecular structures of 2-ethoxyethanol (a), DEG (b) and 1-(2,2,2-trihydroxyethoxy)ethane-2,2,2-triol (c), respectively. The O, C, and H atoms are represented in red, cyan, and silver, respectively.

In order to understand how the chemical structure of the binder phase affects the breaking strength, especially the number of the hydroxyl (OH) groups of the binder species, we compare the breaking strengths using 2-ethoxyethanol, DEG, and 1-(2,2,2-trihydroxyethoxy)ethane-2,2,2-triol as the binder species. The chemical structures of the three species are illustrated in Fig. 2, which contain 1, 2 and 6 hydroxyl groups, respectively. For each binder species, we also prepare 5 cases and carry out NVT-MD simulations for the print, curing, burn-out and sintering stages in each case, respectively. Each case contains 160 water, 60 binder species molecules, and 2 Cr-oxide powders.

Depth-first search algorithm

Depth-first search (DFS) is an algorithm that is used for finding a solution path from a starting node to a goal node.[30,31] As shown in Fig. 3, this search algorithm starts by traversing Edge start-A, exploring one of the successors of the starting node (Node A). At the next step, it explores Node C by traversing Edge A-C. However, Node C is not the goal node and it has no successors. Therefore, the search returns to Node A and subsequently explores Node D, which is the other successor of Node A. The search repeats in this way until all nodes and edges in the graph are searched and out-

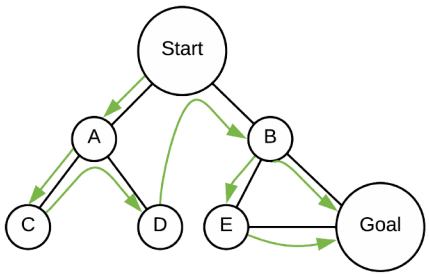

Fig. 3 Depth-first search. The green arrows indicate the searching steps. Eventually, the DFS algorithm outputs two paths from this graph: start-B-goal and start-B-E-goal.

puts the path as long as it hits the goal node.[30,31] This algorithm helps us to investigate the underlying mechanism during the print and curing stages.

Results and Discussions

Evolution during a BJP cycle

So as to understand the chemical and physical mechanisms of a BJP cycle, we compare the equilibrated system of 2 Cr-oxide nanoparticles, 160 water, and 60 DEG molecules at 300 K (print), 393K (curing), 900 K (burn-out) and 1900 K (sintering), respectively. In each simulation, enough time is given to the system, so that the system reaches its equilibrium state, which is verified by tracking the potential energy and the kinetic energy of the system. Figure S7 shows the history of the potential and kinetic energy of each stage. For the print stage, the potential energy of the system reaches equilibrium after 1.5 ns. At the curing stage, the variation of potential energy is more significant. However, the system features no obvious increasing or decreasing trend after 7.5 ns. Besides, the number of dissociated water molecules is stabilized after 7.5 ns. Similarly, neither continuous ascending nor desending trend is featured after 10.5 ns for the burnout stage and 13.5 ns for the sintering stage. Moreover, we remove all dissociated gaseous molecules from the systems at 8.25 ns, 11.25 ns, and 14.25 ns, on which an extra NVT-MD simulation is carried out to verify whether the BJP part reaches the equilibrium state of the curing, burn-out and sintering stages, respectively. Figs. S7h-S7i show that the potential energies of the BJP part are generally stable. Based on these observations, it is suggested that system at 2.5 ns, 8.25 ns, 11.25 ns, and 14.25 ns reaches the equilibrium state of the print, curing, burnout and sintering stages, respectively and is suitable for the characterization of mechanical properties.

The evolution of these four stages is shown in Fig. S4. Our simulations indicate that the water and DEG molecules agglomerate and attach to the surface of the Cr-oxide particles at the print stage. They form a three-dimensional network that links the two Cr-oxide particles. However, the attached DEG and water molecules are unequally distributed on the Cr-oxide surface and not the whole exterior of the Cr-oxide powder is covered. This phenomenon implies that the mechanical properties of a green part are inhomogeneous after the print stage. During curing at 393 K, most water molecules dissociate from the network or the

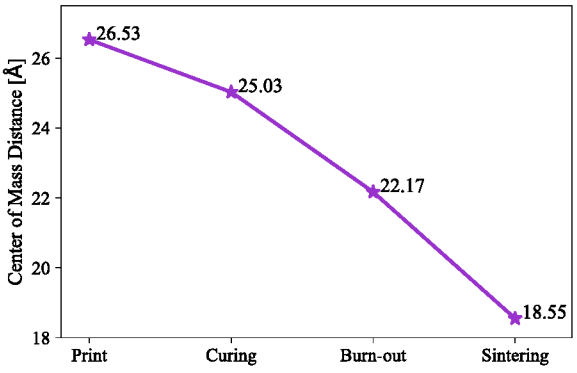

Fig. 4 The development of the center of mass distance between the two Cr-oxide nanoparticles. The mass center distance variation in the next 100 ps after the system reaches equilibrium is less than 1 Å.

Cr-oxide surface. However, the DEG and water molecules remaining in the network after curing continue to connect the two Cr-oxide powders. Meanwhile, some DEG molecules that did not previously participate in bonding Cr-oxide nanoparticles at the print stage enter the space between the two Cr-oxide particles and join the network.

However, the bridging network, which contains water and DEG molecules, breaks down as the temperature is raised to 900 K. The majority of DEG decompose then and are oxidized gradually to small molecules such as CO_2, CH_2O, $C_2H_4O_2$, *etc.* These species are gaseous at 900 K and detach from the Cr-oxide particles. After 3 ns of burning, 48 carbon atoms still remain on the surface of the particles by forming C-O bonds with exterior oxygen atoms of the Cr-oxide. In addition, the two Cr-oxide powders are partially sintered at the burn-out stage, since new Cr-O bonds form between the two Cr-oxide particles. These new Cr-O bonds form a necking between the two Cr-oxide particles. Interestingly, prior to the burn-out treatment, Cr-O bonds bridging the two Cr-oxide nanoparticles were not observed, which means that the two Cr-oxide particles are still independent at both the print and curing stages. At the sintering temperature of 1900 K, more Cr-O bonds are produced and the necking between the two Cr-oxide particles expands. Meanwhile, the carbon atoms, which remain on the powder surface after the burn-out stage, are oxidized gradually with exterior oxygen of the Cr-oxide particles and dissociate. Besides, hydroxyl (OH) groups dissociate from the particles during sintering.

Fig. 4 shows that the center of mass distance of the two Cr-oxide particles decreases gradually. The center of mass distances are calculated at the equilibrium state of each stage. At the print stage, the center of mass distance is approximately 26.53 Å, which declines to 25.03 Å after curing. This distance reaches the minimum of 18.55 Å after sintering. The decline of the center of mass distance indicates the space among Cr-oxide powders is reduced, leading to shrinkage of the part at the macroscopic scale.

In order to compare the breaking strength of each stage, an additional force is applied to separate the two Cr-oxide particles. Un-

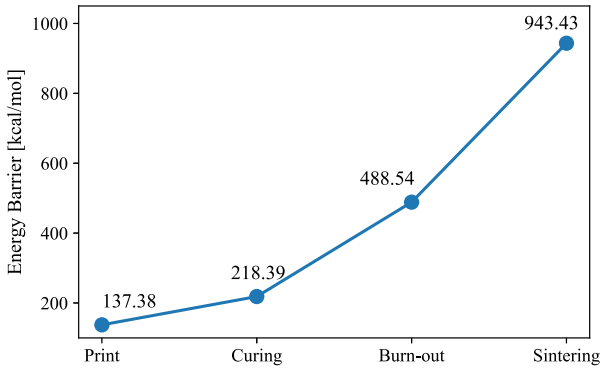

Fig. 5 Energy barriers to separate the two Cr-oxide particles.

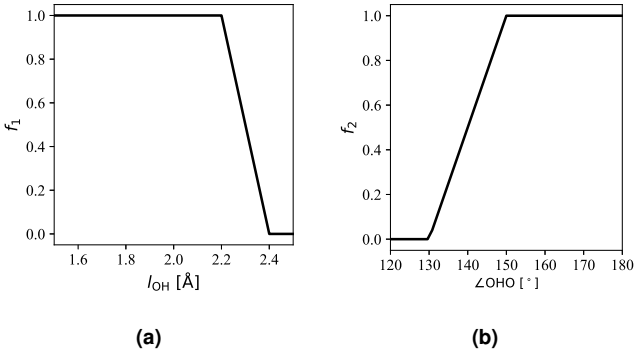

Fig. 6 H-bond definition based on l_{OH} and ∠OHO.

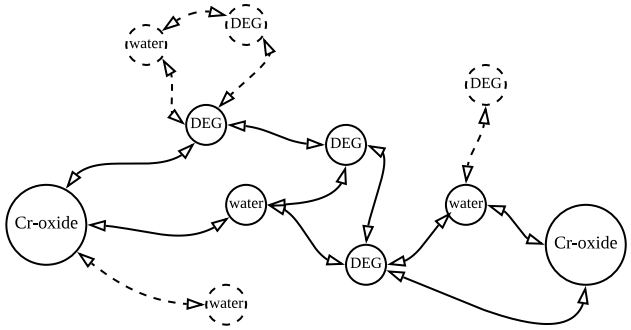

Fig. 7 Schematic of water and DEG molecules associated via H-bonds. The DFS algorithm identifies the "useful" molecules and H-bonds which contribute to bonding the two Cr-oxide particles. The "useful" H-bonds form several continuous paths between the two Cr-oxide nanoparticles. The "useful" molecules are the molecules on those continuous paths. The arrows represent H-bonds. The "useful" molecules and H-bonds are illustrated with solid lines, whereas the "useless" ones are shown with dash lines.

der this external force, the potential energy of a system ascends gradually to its peak and the two Cr-oxide particles subsequently break apart, as shown in Fig. S5. The peak energy or the energy barrier reflects the breaking strength, which are summarized in Fig. 5. The energy barrier for particle separation increases by 81 kcal/mol at the curing stage with respect to the print stage. The highest energy barrier 943.43 kcal/mol is featured after sintering. This trend agrees well with the experiment. [1,2]

Mechanism of the print and curing treatments.

While prior studies have experimentally observed that a green part gains strength after curing, this is the first reported study that shows a network bridging the two Cr-oxide nanoparticles during the print and curing stages, which consists of water and binder species. In the network, the distances of hydrogen (H) and oxygen (O) atoms from different molecules generally range from 1.5 Å to 2.5 Å. Considering the length of a covalent O-H bond is roughly 0.96 Å, we estimate hydrogen bonds (H-bonds) play a crucial role in holding the two Cr-oxide particles during the print and curing stages. There are two challenges to prove this hypothesis: first, a criterium is needed to judge if two water/DEG molecules are bonded via a H-bond. Second, not all H-bonds participate in associating the two Cr-oxide particles: some H-bonds form dangling ends or loops, which do not contribute to strengthening the green part. [32]

Doruker *et al.* [33] defined a H-bond based if the distance of O and H atoms (l_{OH}) is less than 2.3 Å. However, this definition is not accurate since it ignores angular effects and this definition completely neglects H-bond lengths between 2.3 Å and 2.4 Å. [34,35]

In our present work, we set the following three conditions for a H-bond [34,35]: first, 1.5 Å $\leq l_{OH} <$ 2.4 Å (l_{OH} refers to the distance between the H atom and the O atom from another molecule). Here, ±0.1 Å tolerance is described by a linear function (f_1) to account for l_{OH} around 2.3 Å, as shown in Fig. 6a. Second, the valence angle 130° $<$ ∠OHO $\leq$ 180° and another linear function (f_2) is employed for the description of the ±10° variation around 140°, as shown in Fig. 6b. Third, the H atom of a H-bond must form a covalent bond with an O atom, so that the H atom can acquire a significant positive charge to form a dipole-dipole attraction. In contrast, the H atoms connected to the carbon (C) atoms are unable to form a H-bond, since the C atoms are not sufficiently electronegative. A H-bond h_i is summarized as:

$$h_i = \frac{f_1 + f_2}{2}. \quad (4)$$

In order to identify all "useful" H-bonds that participate in connecting the two particles and all "useless" H-bonds, the depth-first search (DFS) algorithm is employed, as illustrated in Fig.7. By removing "useless" molecules detected by the DFS algorithm, we rebuild the bridging network with only "useful" DEG and water molecules as well as the two Cr-oxide particles. The energy barrier to separate the particles in this "useful" system is compared with that of the original system in Fig. 8. In both the original and "useful" systems, the potential energies increase initially and then decrease. Under the exertion of the external force, the H-bond network is stretched. As a result, the potential energy of the system increases gradually. With the energy stored in the H-bond network rises, an increasing number of H-bonds in the network start to break. But the two nanoparticles are seized by the H-bond network. This process continues until the H-bond net-

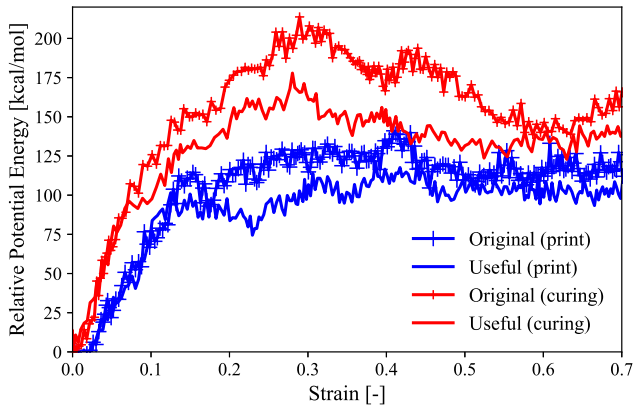

Fig. 8 Comparison of relative potential energy evolution of the original system and the system of "useful" molecules identified by the DFS algorithm.

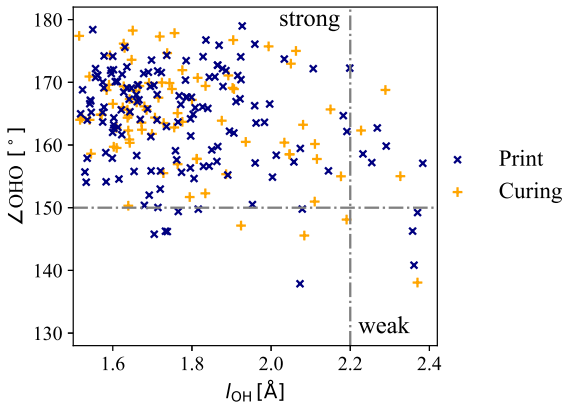

Fig. 9 Comparison of the "useful" H-bonds during the print and curing stages. The x-axis is the H-bond distance l_{OH}. The y-axis is the valence angle ∠OHO.

work reaches a critical point, where enough H-bonds are broken, leading to a separation of the two nanoparticles. Afterwards, the stretched bonds in the system relax, resulting in the decrease of the potential energy. The energy barrier of the original system is 137.38 kcal/mol and 218.39 kcal/mol for the print and curing stages, respectively; while that of the "useful" system is 121.40 kcal/mol and 177.88 kcal/mol, respectively. As such, the energy barrier featured by the "useful" system is only 11.63% (print) and 18.55% (curing) lower than that in the original system. This difference is probably due to the van der Waals forces and other extremely weak H-bonds. Despite such deviations, the relative potential energies of the "useful" system still have a good agreement with those of the original system. This phenomenon confirms the hypothesis that the H-bond network plays a crucial role in bonding the Cr-oxide powders. As the covalent bonds in the network, *e.g.*, O-H bonds and C-O bonds are significantly stronger than H-bonds, the H-bonds break before the covalent bonds. Thus, the breaking strengths at the print and curing stages are dominantly determined by the H-bond network.

Based on this observation, it is necessary to investigate the H-bond network associating the Cr-oxide particles to understand how the curing treatment strengthens a green part. There are three potential causes of this observation:

- The number of "useful" H-bonds is increased after curing.
- The number of strong "useful" H-bonds is elevated by the curing treatment, whereas the number of weak "useful" H-bonds is reduced.
- A "useful" molecule in the H-bond network share more H-bonds with other molecules, making the separation more difficult.

Regarding the first potential cause, we monitor the H-bond network for 100 ps with 10 ps saving frequency after the system reaches equilibrium, considering the flutuation of potential energy at the print and curing stages. The number of "useful" H-bonds is calculated by summarizing all "useful" H-bonds (h_i) detected by the DFS algorithm. The ReaxFF MD simulation results reveal that the amount of "useful" H-bonds decreases sharply after curing. At the print stage, the number of "useful" H-bonds ranges from 115.17 to 158.68. After curing, the number of "useful" H-bonds ranges from 68.32 to 86.26. The loss of H-bonds is caused by the evaporation of water, which also contributes to linking the Cr-oxide particles during the print stage.

Fig. 9 compares the number of strong and weak "useful" H-bonds in the network that associates the Cr-oxide particles at the print and curing stages. The number of the strong H-bonds, whose valence angle ∠OHO is above 150° and the H-bond length l_{OH} is between 1.5 Å and 2.2 Å, is 132 and 78, respectively for the print and curing stages; whereas the corresponding number of the weak H-bonds, whose ∠OHO is below 150° and l_{OH} is above 2.2 Å, is 1.44 and 0.27. Even though the amount of weak "useful" H-bonds is slightly reduced, the number of strong "useful" H-bonds decreases significantly after curing. Thus, this explanation is not plausible.

Regarding the final potential cause, the ratio of the number of "useful" H-bonds to the number of "useful" molecules before curing is compared with that after curing in Tab. 2. The number of "useful" H-bonds and the number of "useful" molecules at the print stage are greater than those after curing. However, the ratio of the number of "useful" H-bonds over the number of "useful" molecules is raised after curing. The rise of the ratio indicates that a molecule in the network shares generally more H-bonds with its neighbors after curing.

On the other hand, Fig. 10 reveals that the water molecules provide approximately 43.3% "useful" H-bonds at the print stage, while this contribution drops to 12.6% at the curing stage due to water evaporation. On the contrary, the proportion of the "useful" H-bonds from DEG and Cr-oxide increases from 24.9% to 44.9%

Table 2 The number of "useful" H-bonds and "useful" molecules and their ratio in 100 ps after the system reaches equilibrium.

	"Useful" H-bonds	"Useful" molecules	Ratio
Print	115.17 ∼ 158.68	47 ∼ 61	2.37 ∼ 2.56
Curing	68.32 ∼ 86.26	21 ∼ 28	2.95 ∼ 3.19

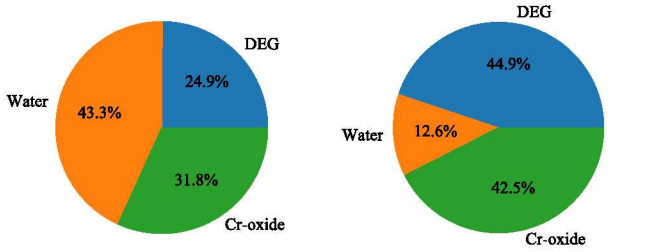

(a) Print **(b)** Curing

Fig. 10 Sources of "useful" H-bonds at the print (a) and curing (b) stages, respectively.

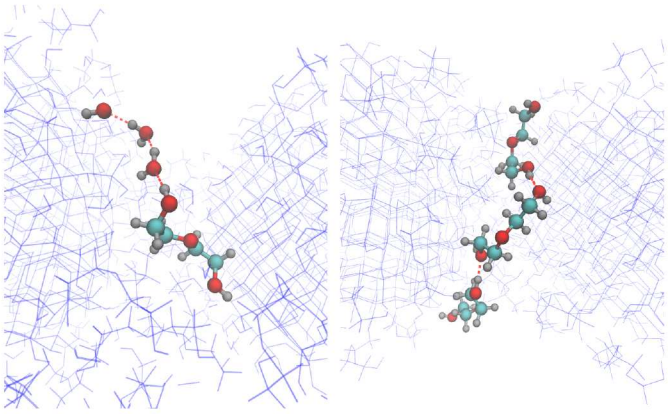

(a) Print **(b)** Curing

Fig. 11 A typical "useful" H-bond chain that associates the two Cr-oxide nanoparticles at the print and curing stages. The H, C and O atoms in the chains are highlighted in silver, cyan, and red, respectively. The chain of the print stage contains more water molecules than that of the curing stage.

and from 31.8% to 42.5%, respectively, indicating that the Cr-oxide nanoparticles are primarily linked by DEG after curing.

Since H-bonds (intermolecular interactions) are substantially weaker covalent bonds (intramolecular interactions), breaking the H-bond network essentially is to separate some molecules from their neighbors. As shown in Fig. 11, the "useful" H-bond chain at the print stage generally contains more water than that at the curing stage. The molecular structure of DEG has two hydroxyl groups at the two ends, therefore, it forms more H-bonds than water with nearby molecules in the network. Hence, the ratio of the number of "useful" H-bonds over the number of "useful" molecules grows and the bridging network is strengthened, as the contribution from DEG increases after curing.

Mechanism of the burn-out and sintering treatments.

The H-bond network breaks down during the burn-out stage. Most DEG molecules decompose and are oxidized gradually to gaseous carbon-containing species (*e.g.*, CO_2, CH_2O, *etc.*). However, 48 carbon atoms remain on the surface of the Cr-oxide powders by forming C-O bonds after 3 ns of burning. Also at the burn-out stage, the two Cr-oxide particles start to merge by forming new Cr-O bonds. During sintering at 1900 K, the formation

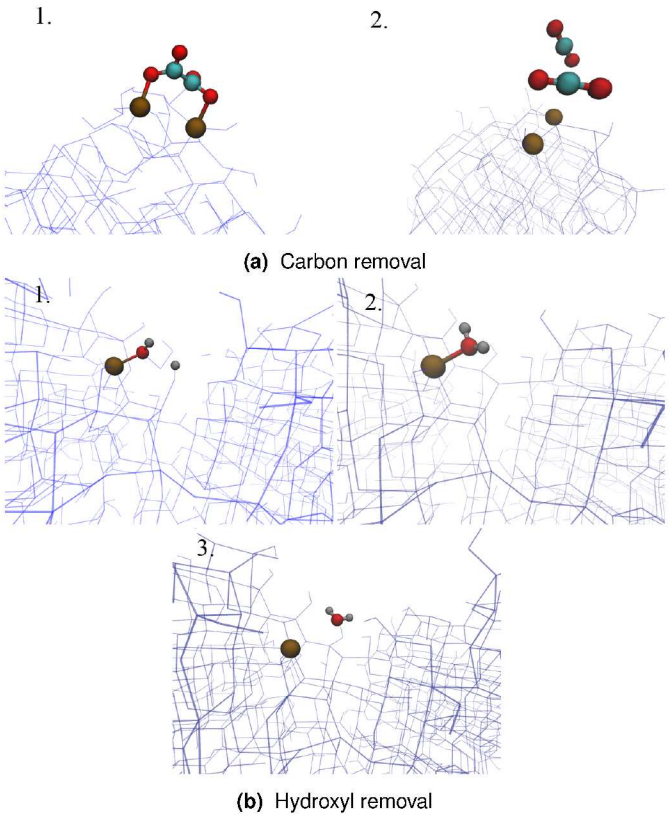

(a) Carbon removal

(b) Hydroxyl removal

Fig. 12 Removal of carbon and hydroxyl groups from the Cr-oxide surface at 1900 K. The C, Cr, O, and H atoms are highlighted in cyan, ochre, red and silver, respectively.

of Cr-O bonds accelerates extensively. Interestingly, the remaining 48 carbon atoms dissociate gradually from Cr-oxide particles. As shown in Fig. 12a, the Cr-O bonds of the two surface oxygen atoms (red) that were connected with carbon atoms (cyan) before sintering, break at 1900 K, producing two CO_2. Additionally, hydroxyl groups dissociate from the Cr-oxide surface at 1900 K by forming water molecules or hydroxyl radicals. Fig. 12 illustrates the process of hydroxyl removal. As a nearby H atom approaches an OH group on the surface of the Cr-oxide particle, they form an H_2O molecule, which subsequently dissociates from the Cr-oxide surface. Alternatively, it is observed that hydroxyl groups leave the Cr-oxide surface without forming water molecules at 1900 K. Both the removal of carbon atoms and hydroxyl groups continuously reduce the surface oxygen of the Cr-oxide powders and create an oxygen vacancy. As a result, an increasing number of Cr atoms on the Cr-oxide surface become active and could form Cr-O bonds with O atoms from the other Cr-oxide nanoparticle. Fig. 13 compares the newly formed bridging Cr-O bonds between the two Cr-oxide nanoparticles during the burn-out and sintering stages. In order to calculate the number of new Cr-O bonds between particles, the molecular label of each atom must be recorded since the two Cr-oxide nanoparticles are independent (prior to the burn-out stage). For each O atom, we check the source of its connected Cr-atoms (Namely, by which nanoparticle the Cr atom is provided). If its connected Cr

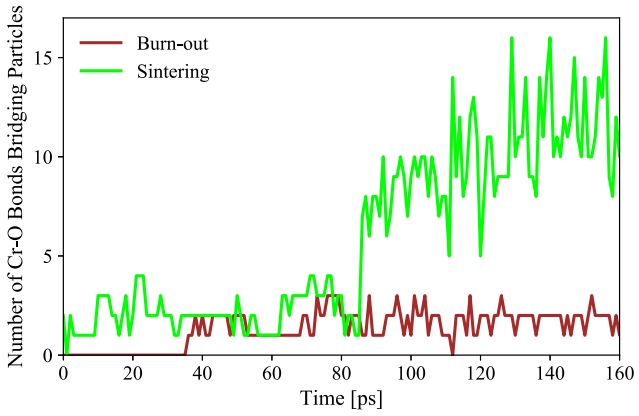

Fig. 13 Number of newly formed Cr-O bonds bridging the two Cr-oxide nanoparticles. At time 0, the temperature of the burn-out and sintering stages is increased to 900 K and 1900 K, respectively.

atoms are all from the same nanoparticle, none of its Cr-O bonds is the newly formed Cr-O bond between nanoparticles. If the connected Cr atoms are from different nanoparticles, the number of the new bridging Cr-O bonds is calculated by counting the bonds between the O atom and the connected Cr atoms from the other nanoparticle. As shown in Fig. 13, up to 3 Cr-O bonds linking the two nanoparticles are produced within the initial 160 ps of the burn-out stage, which implies that the Cr-oxide nanoparticles are partially sintered. During sintering, the formation of new bridging Cr-O bonds between the Cr-oxide particles accelerates significantly after the initial 80 ps and maximally 16 bridging Cr-O bonds form between the two Cr-oxide nanoparticles.

Influence of binder solution composition

Understanding the influence of binder solution composition on mechanical properties is essential to improve BJP technology. Previous research in this area indicated that the strength of a green part at the print and curing stages is improved by a higher saturation ratio, while excess saturation weakens the sintered sample.[12–15] But it should be noted that a higher saturation ratio can be achieved by adding either water or binder species. Unfortunately, no reported studies have done to help us understand the roles of water and binder phase in a BJP process. For that, we define two sets of simulations that control the amount of water and DEG molecules independently, as shown in Tab. 1.

Fig. 14 compares the average energy barrier and error bar for each binder solution composition after the print, curing, burn-out and sintering treatments, respectively. At the print and curing stages, an increasing number of both water and DEG molecules lead to a higher average energy barrier. At the burn-out and sintering stages, the influence of water on the mean energy barriers is not obvious. In contrast, the mean energy barrier after sintering of 60 DEG in Set B is 228.49 kcal/mol higher than that of 100 DEG, and 442.57 kcal/mol higher than that of 20 DEG. Besides, it is evident from Fig. 14a that a smaller error bar of energy barriers at the print and curing stages can be achieved with fewer water molecules. On the other hand, the largest error bar in Set B at

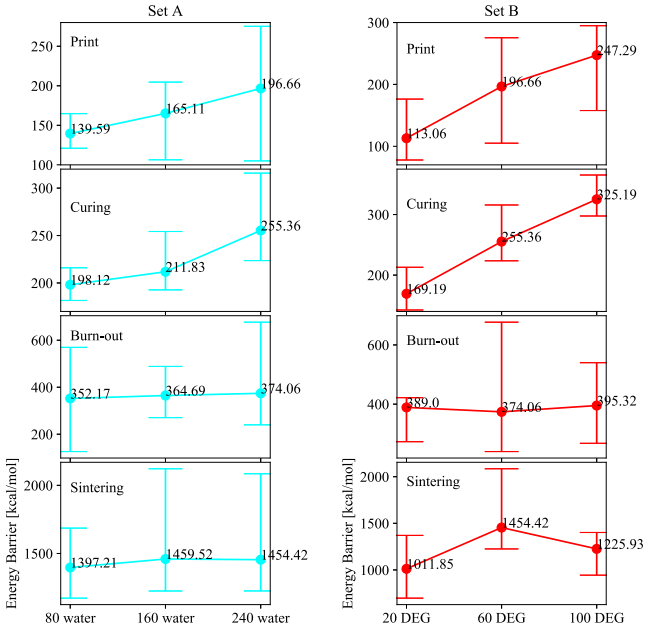

Fig. 14 Mean energy barriers and error bars for each binder solution composition.

the print (170.20 kcal/mol) and curing stages (92.17 kcal/mol) is featured in 60 DEG, even though the mean energy barrier of 60 DEG is not the highest. Interestingly, the error bar of energy barriers after curing drops by approximately 21.3%, 41.2%, and 45.8%, respectively for 80, 160 and 240 water molecules in Set A, and by 28.4%, 45.8%, and 50.6%, respectively for 20, 60 and 100 DEG molecules in Set B; suggesting that the homogeneity of the green part is improved during curing for each binder solution composition. However, the error bars of energy barriers in both Set A and Set B grow significantly during the burn-out stage and reach the maxima after sintering. The augmentation of error bars indicates that the product becomes extremely inhomogeneous especially after sintering.

In order to understand the underlying mechanism for the strength variation in Set A, Fig. 15 compares the ratio of the number of “useful" H-bonds over the number of “useful" molecules (a) as well as the number of “useful" H-bonds (b). Interestingly, Fig. 15a demonstrates no obvious correlations between the mean energy barrier and the ratio of the number of “useful" H-bonds to the number of “useful" molecules. However, Fig. 15b reveals a positive correlation between the average number of “useful" H-bonds and the average energy barrier, since the number of “useful" H-bonds increases, as the energy barrier ascends.

From Fig. 16a, no apparent correlations between the average energy barrier and the average ratio of the number of “useful" H-bonds to the number of “useful" molecules can be identified in Set B. From Fig. 16b, a similar positive correlation between the average number of “useful" H-bonds and the average energy barriers also exists in Set B. The number of “useful" H-bonds increases with the growth of the energy barrier.

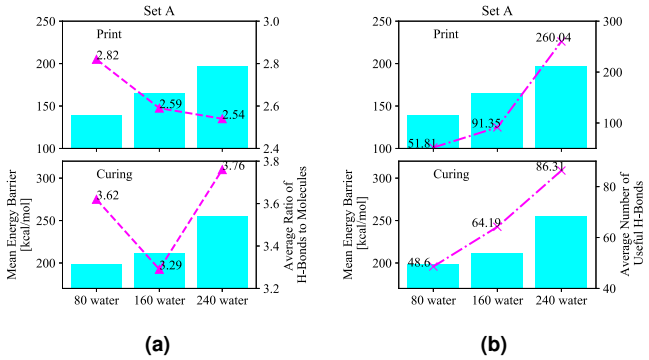

Fig. 15 Comparison of the H-bond networks in Set A. The mean energy barriers are depicted in cyan, whereas the ratio of the number of "useful" H-bonds over the number of "useful" molecules as well as the "useful" H-bonds amount is illustrated in pink.

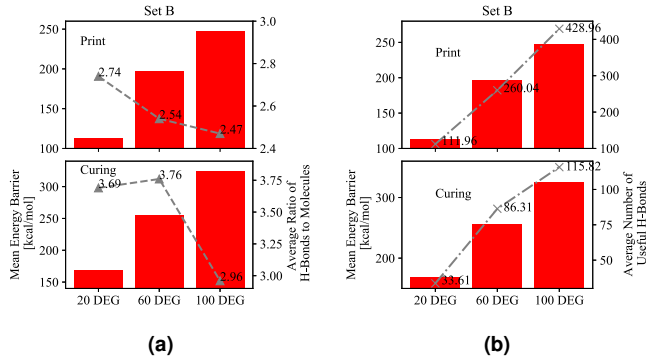

Fig. 16 Comparison of the H-bond networks in Set B. The mean energy barriers are depicted in red, whereas the ratio of the number of "useful" H-bonds over the number of "useful" molecules and the "useful" H-bonds amount are illustrated in grey.

The average "useful" H-bond contributions of water, DEG and Cr-oxide nanoparticles are compared in Tab. 3. It is evident from Tab. 3 that adding both water and DEG can promote the "useful" H-bond formation of DEG and Cr-oxide nanoparticles at the print and curing stages; since the "useful" H-bonds provided by DEG and Cr-oxide increase at the print and curing stages with the growth of the number of water or DEG molecules. Moreover, the average number of "useful" H-bonds provided by water at the print stage is also elevated by adding water or DEG molecules. After curing, however, the difference of the "useful" H-bond contributions of water among all three compositions is comparable with those of DEG and Cr-oxide in Set A but is less significant than those of DEG and Cr-oxide in Set B.

Based on this analysis, two features of the H-bond network affect the breaking strength of green parts at the print and curing stages. The first feature is the number of "useful" H-bonds. Increasing saturation with more water/DEG molecules contributes to more "useful" H-bonds that link powders during the print and curing stages. The second feature is the ratio of the number of "useful" H-bonds over the number of "useful" molecules. During curing, the ratio of the number of "useful" H-bonds over the number of "useful" molecules is elevated, which indicates that the molecules are more firmly trapped in the H-bond network among powders. Consequently, breaking the network becomes more difficult.

Fig. 17 compares the average number of the new bridging Cr-O bonds between the two Cr-oxide nanoparticles after sintering for each composition. As shown in Fig. 17, the number of the new bridging Cr-O bonds qualitatively reflect the breaking strength after sintering, especially in Set B. The composition of 60 DEG plus 240 water molecules, which exhibits the highest breaking strength in Set B, shows 32.8 newly formed Cr-O bonds between the two nanoparticles on average, whereas the 20 DEG-240 water-combination, which features the weakest breaking strength, also demonstrates the fewest bridging Cr-O bonds (25.6). It should be noted that Cr-O-O bonds are not stable at high temperature,[11,36] the bridging oxygen bonds (Cr-O-Cr) are therefore more favorable during sintering. Actually, no Cr-O-O-Cr bonds are observed between the two Cr-oxide nanoparticles at 1900 K in our simulations. Thus, we focus on the number of bridging Cr-O bonds.

The discrepancies of breaking strengths among different compositions in Set B after sintering might be caused by two factors. On one hand, Cr-oxide nanoparticles in our ReaxFF MD simulations are not spherically symmetric. As a result, the contact area of the two Cr-oxide particles may vary significantly, where new bridging Cr-O bonds are produced. Larger contact area generally produces more Cr-O bonds between the two nanoparticles and the energy barrier is hence higher. It is possible that the average contact area of the Cr-oxide nanoparticles in 60 DEG is accidentally larger than its counterparts. Alternatively, the breaking energy barrier difference is possibly due to the variation of surface oxygen content. The removal of carbon and terminal hydroxyl groups on the surface of the Cr-oxide powders continuously reduces the surface oxygen and creates oxygen vacancies, which simultaneously creates active Cr atoms. However, surface oxygen is necessary to form a bridging Cr-O bond. Therefore, over-

Table 3 Average "useful" H-bond contributions from water, DEG and Cr-oxide nanoparticles

		SetA			SetB		
		80 water	160 water	240 water	20 DEG	60 DEG	100 DEG
Print	water	11.50	33.07	127.15	62.13	127.15	194.00
	DEG	19.79	27.31	54,72	9.61	54.72	120.71
	Cr-oxide	20.52	30.97	78.71	40.23	78.17	114.25
	sum	51.81	91.35	260.04	111.96	260.04	428.96
Curing	water	4.45	7.32	11.80	4.71	11.80	10.40
	DEG	20.72	27.42	31.88	6.92	31.88	59.64
	Cr-oxide	23.43	29.40	42.62	21.98	42.62	45.77
	sum	48.60	64.19	86.31	33.61	86.31	115.82

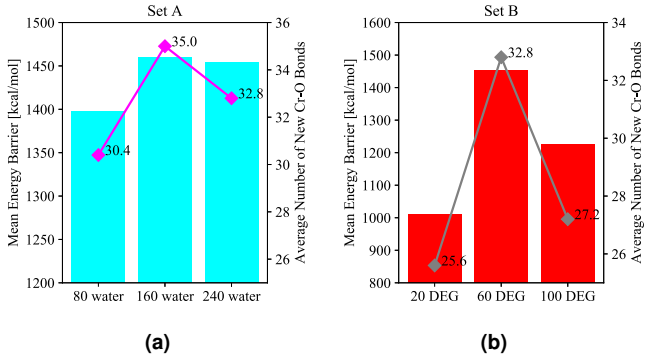

Fig. 17 Comparison of the number of newly formed Cr-O bonds between the two sintered Cr-oxide powders. The mean energy barriers of Set A and Set B are shown in cyan and red, respectively, while the mean number of new Cr-O bonds are presented in pink and grey, respectively. It should be noted that the number of new bridging Cr-O bonds provides only a rough estimate of the breaking strength, because this number does not account for the bond order variation among the bridging Cr-O bonds.

consumption of the surface oxygen can also limit the formation of Cr-O bonds bridging the two Cr-oxide powders. Under this trade-off, there is an optimum quantity for the binder solution. In fact, the average number of surface oxygens after sintering declines by approximately 50, as the number of DEG increases from 20 to 100. Although the experimental observation that oversaturation results in lower rupture strength after sintering is reproduced in our ReaxFF MD simulations, more investigations must be done to completely understand the influence mechanisms of binder species on the mechanical properties of sintered parts. This is because, in addition to the reduction reactions on powder surfaces, binder species in experiments affect the formation of carbides and Laves phase in sintered samples, which involve elements including Ni/Mo/Mn/Ti/Nb/Fe, etc.[1,9,37–39] The carbides and Laves phase can significantly alter the mechanical properties. In the ReaxFF MD simulations presented in this work, however, the powder surfaces are pure Cr-oxide and we set no bond interactions between Cr and C atoms in the force field.[11] Hence, there are no carbides or Laves phase at 1900 K in our simulations. In the future, more elements will be introduced into the force field, so that we are able to capture the influences of carbides and Laves phase on the mechanical properties of a BJP product.

Influence of hydroxyl groups

In the previous section, we discovered that H-bonds play a crucial role in determining the strength of a green part at the print and curing stages. A H-bond is constituted with a donor X-H and an acceptor A.[40–42] The element X must be sufficient electronegative to form a dipole moment with H. In the environment of water, DEG and Cr-oxide, only the hydroxyl group fulfills this requirement. Therefore, the number of hydroxyl groups of the binder species is expected to affect the mechanical properties of a green part. Based on this observation, we investigate 2-ethoxyethanol with a single hydroxyl group, DEG with two hydroxyl groups, and 1-(2,2,2-trihydroxyethoxy)ethane-2,2,2-triol with six hydroxyl groups.

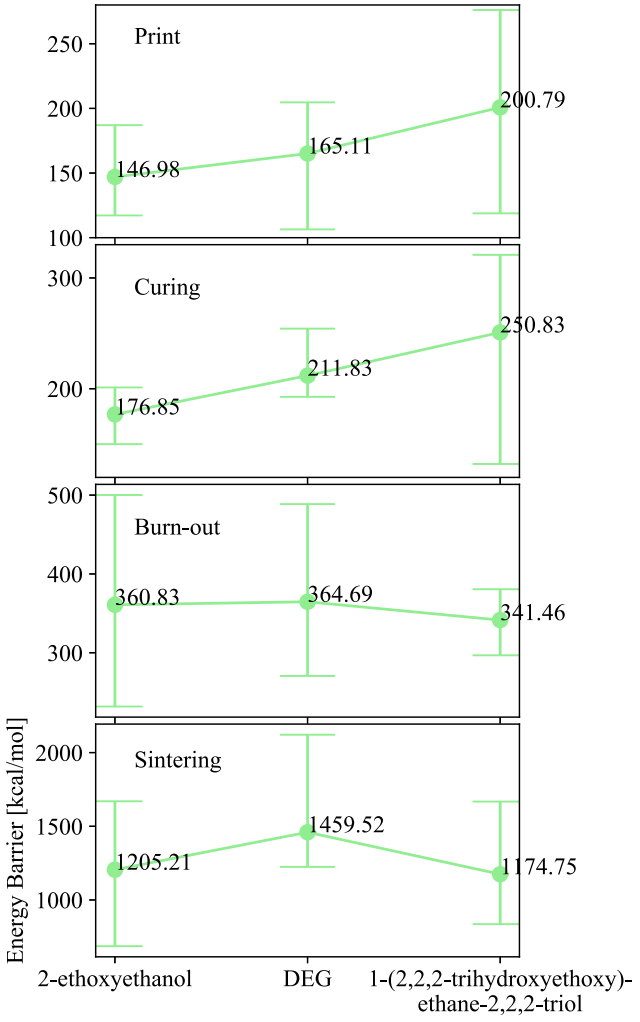

Fig. 18 Mean energy barriers and error bars of 2-ethoxyethanol, DEG and 1-(2,2,2-tri-hydroxyethoxy)ethane-2,2,2-triol.

Fig. 18 compares the energy barriers for particle separation and the error bars using all three species as the binder phase. At the print stage, 1-(2,2,2-trihydroxyethoxy)ethane-2,2,2-triol shows the highest average energy barrier 200.79 kcal/mol, while 2-ethoxyethanol features the lowest one 146.98 kcal/mol. After curing, the highest mean energy barrier 250.83 kcal/mol is also observed in 1-(2,2,2-trihydroxyethoxy)ethane-2,2,2-triol. This value is approximately 38.98 kcal/mol and 74.00 kcal/mol higher than that demonstrated in DEG and 2-ethoxyethanol, respectively. The difference of the mean energy barriers among the three species confirms that increasing the number of hydroxyl groups in the binder phase enhances the breaking strength of a green part at the print and curing stages. Additionally, the error bars of the energy barriers of 1-(2,2,2-tri-hydroxyethoxy)ethane-2,2,2-triol at the print and curing stages are significantly larger than those of DEG and 2-ethoxyethanol. This implies that the mechanical properties of the green part at the print and curing stages are more

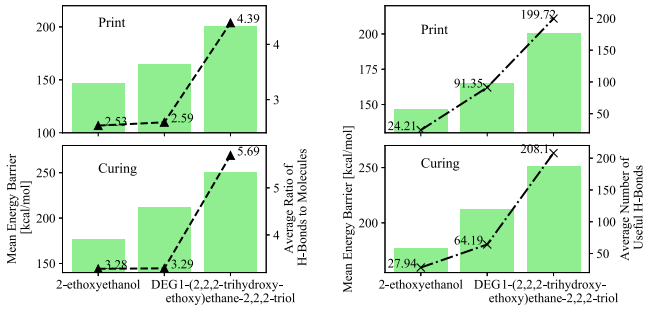

Fig. 19 Comparison of the H-bond network of 2-ethoxyethanol, DEG and 1-(2,2,2-tri-hydroxyethoxy)ethane-2,2,2-triol. The mean energy barriers are depicted in light green, whereas the average ratio of the number of "useful" H-bonds over the number of "useful" molecules as well as the "useful" H-bonds amount is highlighted in black.

inhomogeneous using 1-(2,2,2-tri-hydroxyethoxy)ethane-2,2,2-triol than using DEG or 2-ethoxyethanol. A molecule with more hydroxyl groups forms more H-bonds with nearby molecules. Therefore, the spreading of the binder species with numerous hydroxyl groups becomes increasingly difficult. In fact, the Ohnesorge number (Oh) of the binder solution, which is a parameter demonstrating the ratio of fluid viscosity over inertial and surface forces, is required to be smaller than 1.[1,43] At the burn-out stage, the mean energy barriers of all three binder species are nearly identical. Meanwhile, the error bar in DEG and 2-ethoxyethanol rises significantly to 268.41 kcal/mol and 217.90 kcal/mol, respectively, whereas that of 1-(2,2,2-trihydroxyethoxy)ethane-2,2,2-triol decreases from 188.76 kcal/mol to 83.82 kcal/mol. The mean energy barriers and the error bars of all three binder species achieve the maxima after sintering. Among them, the highest mean energy barrier is featured in DEG, which is roughly 254.32 kcal/mol higher than that in 2-ethoxyethanol, and 284.77 kcal/mol higher than that in 1-(2,2,2tri-hydroxyethoxy)ethane-2,2,2-triol. Similarly, the greatest error bar of the energy barriers is featured also in DEG and is 194.77 kcal/mol and 346.08 kcal/mol larger than that in 2-ethoxyethanol and 1-(2,2,2-tri-hydroxyethoxy)ethane-2,2,2-triol, respectively.

Fig. 19 compares the average ratio of the number of "useful" H-bonds over the number of "useful" molecules (a) as well as the average number of "useful" H-bonds (b). Apparently, the average number of "useful" H-bonds and the average ratio of the number of "useful" H-bonds over the number of "useful" molecules are elevated, as the number of OH groups in the molecular structure of binder species increases. Interestingly, the average number of "useful" H-bonds increases slightly after curing for 2-ethoxyethanol and 1-(2,2,2-trihydroxyethoxy)ethane-2,2,2-triol in spite of water evaporation. This increase is due to the facilitated spreading of the binder species during curing. As shown in Fig. S6, some binder species and water molecules accumulate on the top of the left particle at the print stage, which do not participate in linking the two Cr-oxide nanoparticles. Curing at 393 K increases the kinetic energies of the binder species. As a result, many binder molecules overcome the energy barrier of migration and move into the space between the two Cr-oxide nanoparticles, forming a "useful H-bond network between them. Besides, both the ratio of the number of "useful" H-bonds over the number of "useful" molecules and the number of "useful" H-bonds increase non-linearly with the number of hydroxyl groups in the molecular structure of the binder species. This is probably because water and Cr-oxide, the quantity of which is kept constant for each case, also provide "useful" H-bonds.

Tab. 4 compares the average "useful" H-bonds contributions of water, binder phase and Cr-oxide using all three binder species. Obviously, the importance of the binder phase in the network is improved with the growth of the number of OH groups in the molecular structure of the binder species. At the print stage, 2-ethoxyethanol provides 13.1%, DEG provides 29.9%, and 1-(2,2,2-tri-hydroxyethoxy)ethane-2,2,2-triol provides 51.7% "useful" H-bonds on average. After curing, 2-ethoxyethanol, DEG and 1-(2,2,2-trihydroxyethoxy)ethane-2,2,2-triol provides 17.5%, 42.8%, and 59.2% "useful" H-bonds, respectively. On the other hand, the "useful" H-bond formation of Cr-oxide at the print and curing stages is also promoted by increasing the number of OH groups in the molecular structure of the binder species, since the average number of "useful" H-bonds provided by Cr-oxide before and after curing is elevated significantly as the number of OH groups in the binder species increases.

Fig. 20 demonstrates the average number of new Cr-O bonds bridging the two nanoparticles after sintering. Apparently, an increasing number of Cr-O bonds linking the two Cr-oxide nanoparticles leads to higher breaking strength. The variation of the breaking strengths between different binder species is possibly due to the powder shapes. Another potential cause is the different surface oxygen consumption through especially the carbon oxidation. Because a 1-(2,2,2-trihydroxyethoxy)ethane-2,2,2-triol molecule has more oxygen in its molecule structure than the other two species, its oxidation consumes less surface oxygen of the Cr-oxide powders, whose amount is a trade-off for the bridging Cr-O bonds formation. However, more research regarding the underly-

Table 4 Average "useful" H-bonds contributions from water, binder phase, and Cr-oxide nanoparticles

		2-ethoxyethanol	DEG	1-(2,2,2-tri-hydroxyethoxy)ethane-2,2,2-triol
Print	water	10.84	33.07	42.68
	binder phase	3.18	27.31	102.01
	Cr-oxide	10.19	30.97	55.03
	sum	24.21	91.35	199.72
Curing	water	8.65	7.32	16.89
	binder phase	4.88	27.47	123.19
	Cr-oxide	14.41	29.40	68.02
	sum	27.94	64.19	208.10

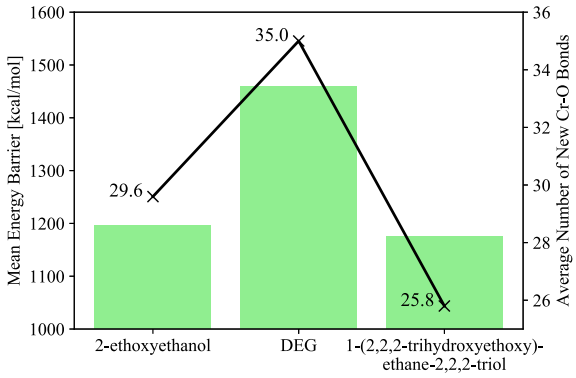

Fig. 20 Comparison of the number of newly formed Cr-O bonds between the two sintered Cr-oxide nanoparticles. The bar diagram demonstrates the mean energy barriers. The mean number of new Cr-O bonds are presented with the black line.

ing mechanism is required in the future.

Conclusions and Outlooks

In the present work, we propose a model for the BJP process based on the ReaxFF reactive force field method. The model is applied to investigate the evolution of AISI 316 L stainless steel powders during a BJP cycle. We first prepare a BJP system using 2 Cr-oxide nanoparticles, 160 water, and 60 DEG molecules and perform NVT-MD simulation at 300 K, 393 K, 900 K, and 1900 K to simulate the print, curing, burn-out and sintering stages, respectively. Results indicate that the water and DEG molecules first agglomerate and attach to the surface of the Cr-oxide nanoparticles inhomogeneously at the print stage. They form a H-bond network that bonds the two Cr-oxide nanoparticles. During curing, many water molecules evaporate, while the DEG molecules remain in the H-bond network. This H-bond network starts to break down as the temperature is elevated to 900 K. Most DEG molecules decompose and are oxidized to gaseous species, however, a small number of carbon atoms are absorbed by the surface oxygen of the Cr-oxide nanoparticles. Subsequently, the two Cr-oxide powders start to merge by forming Cr-O bonds between them at the burn-out stage. During sintering, the remaining carbon atoms are oxidized gradually by the surface oxygen. Furthermore, hydroxyl groups on the surface dissociate from Cr-oxide by attracting nearby hydrogen atoms and forming water molecules subsequently. On rare occasions, they directly escape from the Cr-oxide particles as hydroxyl radicals. Both the carbon oxidation and dehydrogenation continuously reduce the surface of the Cr-oxide and create oxygen vacancies on the surface of powders. During sintering, the formation of the Cr-O bonds accelerates significantly, which bridge the two Cr-oxide nanoparticles. Consequently, the breaking strength is extensively improved after sintering. During a BJP cycle, the distance between the mass centers of the two Cr-oxide nanoparticles declines gradually, suggesting a shrinkage and densification of the BJP sample. In addition, the energy barriers of particle separation at different stages are compared, which reflect the breaking strengths during the BJP process. According to our simulations, the energy barrier of the green sample after curing is improved with respect to the print stage. The highest strength is featured after sintering. This increasing trend agrees well with the trend observed in experiments.[1,2] At the print and curing stages, the "useful" H-bond network plays a crucial role in bonding the two Cr-oxide particles. All DEG/water molecules and the H-bonds in this "useful" network contribute directly to bonding the two Cr-oxide nanoparticles. After curing, the ratio of the number of "useful" H-bonds over the number of "useful" molecules in the network rises, indicating that a "useful" molecule in the network generally shares more H-bonds with its nearby molecules. Hence, this molecule is more firmly trapped in the network after curing. As a result, breaking the H-bond network requires higher energy.

Additionally, we define two sets of simulations to investigate the influence of water and DEG on breaking strengths independently. We perform 5 NVT-MD simulations on each composition and compare their mean energy barrier and error bar. Results demonstrate that the energy barrier can be improved by adding either water or DEG. This trend agrees with the experimental observation that a higher level of binder saturation leads to a higher strength of the green sample at the print and curing stages.[12–14] A comparison of the "useful" H-bond network of each chemical composition reveals a positive correlation between the number of "useful" H-bonds and the energy barrier that reflects the breaking strength. Therefore, both the ratio of the number of "useful" H-bonds over the number of "useful" molecules and the number of "useful" H-bonds can affect the breaking strength before and after curing. On the other hand, the error bar of energy barriers is reduced in each chemical composition after curing, suggesting that the curing treatment improves the homogeneity of the green part. Nevertheless, the error bars grow again at the burn-out stage and reach the maxima after sintering, suggesting that a BJP product becomes most inhomogeneous after sintering if no secondary operation of infiltration is employed. Interestingly, the average energy barriers at the burn-out stage are similar in both sets. After sintering, the mean energy barrier in 60 DEG is the highest. More investigations are needed to understand the cause of such a discrepancy.

Finally, since the H-bonds are crucial in determining the breaking strength at the print and curing stages, we investigate 2-ethoxyethanol, DEG, and 1-(2,2,2-tri-hydroxyethoxy)ethane-2,2,2-triol as the binder species so that we can understand the importance of hydroxyl groups. At both the print and curing stages, the mean energy barrier grows as the number of OH groups in the molecular structure of the binder species increases. Because an increasing number of OH groups significantly promotes the "useful" H-bonds formation of the binder phase and Cr-oxide. However, the error bar in 1-(2,2,2-tri-hydroxyethoxy)ethane-2,2,2-triol is significantly higher than those of its counterparts at the print and curing stages, implying that the green part is most inhomogeneous using 1-(2,2,2-trihydroxyethoxy)ethane-2,2,2-triol as the binder species.

Even though the binder species in our current simulations do not participate directly in the bonding of powders, especially after sintering, their oxidation and dehydrogenation reactions alter the chemical characteristics of the surface of powders, which can fur-

ther affect the formation of the bridging Cr-O bonds among powders. However, the extent of the influence of these two reactions needs to be investigated in the future. Moreover, we will continue to improve our force field and incorporate elements *e.g.*, Fe/Nb/Ti/Ni/Mn/Mo, *etc*. into our force field for simulating a more complexing and realistic BJP process. An accurate force field with numerous elements will provide us a deeper understanding of the BJP process involving carbides and Laves phase *etc*.

Conflicts of interest

The authors declare no competing financial interest.

Acknowledgements

The authors would like to thank the support from the ICS Seed Grant Program of the Pennsylvania State University.

Notes and references

1 P. Nandwana, A. M. Elliott, D. Siddel, A. Merriman, W. H. Peter and S. S. Babu, *Current Opinion in Solid State and Materials Science*, 2017.

2 T. Do, P. Kwon and C. S. Shin, *International Journal of Machine Tools and Manufacture*, 2017.

3 A. Elliott, S. AlSalihi, A. L. Merriman and M. M. Basti, *American Journal of Engineering and Applied Sciences*, 2016.

4 E. O. Garzón, J. L. Alves and R. J. Neto, Advanced Structured Materials, 2017.

5 H. Miyanaji, S. Zhang and L. Yang, *International Journal of Machine Tools and Manufacture*, 2018.

6 M. Doyle, K. Agarwal, W. Sealy and K. Schull, Procedia Manufacturing, 2015.

7 J. Moon, J. E. Grau, V. Knezevic, M. J. Cima and E. M. Sachs, *Journal of the American Ceramic Society*, 2004.

8 T. Ohmi, Y. Nakagawa, M. Nakamura, A. Ohki and T. Koyama, *Journal of Vacuum Science & Technology A: Vacuum, Surfaces, and Films*, 2002, **14**, 2505–2510.

9 P. Lowery, U. Instruments, D. Roll and A. Pak, *Micro-Santa Monica*, 1998, 1–11.

10 P. Stefanov, D. Stoychev, M. Stoycheva and T. Marinova, *Materials Chemistry and Physics*, 2000.

11 Y. K. Shin, H. Kwak, A. V. Vasenkov, D. Sengupta and A. C. van Duin, *ACS Catalysis*, 2015, **5**, 7226–7236.

12 M. Vaezi and C. K. Chua, *International Journal of Advanced Manufacturing Technology*, 2011.

13 M. Xia, B. Nematollahi and J. Sanjayan, *Materials Science Forum*, 2018, **939**, 177–183.

14 Y. Bai and C. B. Williams, *Solid Freeform Fabrication Proceedings*, 2017.

15 S. Shrestha and G. Manogharan, *JOM*, 2017.

16 T. P. Senftle, S. Hong, M. M. Islam, S. B. Kylasa, Y. Zheng, Y. K. Shin, C. Junkermeier, R. Engel-Herbert, M. J. Janik, H. M. Aktulga, T. Verstraelen, A. Grama and A. C. van Duin, *The ReaxFF reactive force-field: Development, applications and future directions*, 2016.

17 J. A. Harrison, J. D. Schall, S. Maskey, P. T. Mikulski, M. T. Knippenberg and B. H. Morrow, *Review of force fields and intermolecular potentials used in atomistic computational materials research*, 2018.

18 A. C. van Duin, S. Dasgupta, F. Lorant and W. A. Goddard, *Journal of Physical Chemistry A*, 2001.

19 T. T. Järvi, A. Kuronen, M. Hakala, K. Nordlund, A. C. van Duin, W. A. Goddard and T. Jacob, *European Physical Journal B*, 2008.

20 J. E. Mueller, A. C. van Duin and W. A. Goddard, *Journal of Physical Chemistry C*, 2010.

21 A. Mostafaei, J. Toman, E. L. Stevens, E. T. Hughes, Y. L. Krimer and M. Chmielus, *Acta Materialia*, 2017.

22 D. Frenkel and B. Smit, *Understanding Molecular Simulation: From Algorithms to Applications (Vol. 1)*, 2001.

23 M. P. Paranthaman, C. S. Shafer, A. M. Elliott, D. H. Siddel, M. A. McGuire, R. M. Springfield, J. Martin, R. Fredette and J. Ormerod, *JOM*, 2016.

24 M. Ziaee, E. M. Tridas and N. B. Crane, *JOM*, 2017.

25 L. Li, B. Post, V. Kunc, A. M. Elliott and M. P. Paranthaman, *Scripta Materialia*, 2017.

26 Ritu, *IOSR Journal of Applied Chemistry Ver. I*, 2015, **8**, 5–11.

27 U. Balachandran, R. W. Siegel, Y. X. Liao and T. R. Askew, *Nanostructured Materials*, 1995.

28 W. D. Callister, M. L. Johnson, I. B. Cutler and R. W. Ure, *Journal of the American Ceramic Society*, 1979.

29 A. C. van Duin, *ReaxFF User Manual*, 2002.

30 R. Tarjan, *SIAM Journal on Computing*, 2005.

31 V. N. Rao and V. Kumar, *International Journal of Parallel Programming*, 1987, **16**, 470–499.

32 R. J. Young and P. A. Lovell, *Introduction To Polymers Third Edition*, 2011.

33 P. Doruker and I. Bahar, *Biophysical Journal*, 1997.

34 M. Golkaram, Y. K. Shin and A. C. T. van Duin, *The Journal of Physical Chemistry B*, 2014, **118**, 13498–13504.

35 E. E. Kwan, *Introduction to Hydrogen Bonding*, 2009.

36 G. V. Chertihin, W. D. Bare and L. Andrews, *Journal of Chemical Physics*, 1997.

37 J. López-Cuevas, J. L. Rodríguez-Galicia, J. C. Rendón-Angeles, M. I. Pech-Canul and J. Méndez-Nonell, *MRS Proceedings*, 2011.

38 J. H. Hsieh, R. Lee, R. A. Erck, G. R. Fenske, Y. Y. Su, M. Marek and R. F. Hochman, *Surface and Coatings Technology*, 1991, **49**, 83–86.

39 G. X. Shen, Y. C. Chen and C. J. Lin, *Thin Solid Films*, 2005.

40 M. Palusiak and S. J. Grabowski, *Journal of Molecular Structure*, 2002.

41 R. Chidambaram and M. Ramanadham, *Physica B: Physics of Condensed Matter*, 1991.

42 G. R. Desiraju and T. Steiner, *The Weak Hydrogen Bond: In Structural Chemistry and Biology*, 1999.

43 B. Derby, *Annual Review of Materials Research*, 2010.

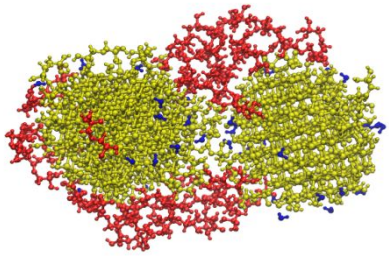

This manuscript is, according to our knowledge, the first reported molecular-level study of BJP technology via molecular dynamics.